Monthly Notices
of the
ROYAL ASTRONOMICAL SOCIETY

MNRAS **512,** 4484–4502 (2022)
Advance Access publication 2022 March 17

https://doi.org/10.1093/mnras/stac744

Close, bright, and boxy: the superluminous SN 2018hti

A. Fiore [1,2★] S. Benetti [2★] M. Nicholl,[3,4] A. Reguitti [2,5,6] E. Cappellaro,[2] S. Campana,[7] S. Bose [8,9] E. Paraskeva,[10,11,12,13] E. Berger,[14] T. M. Bravo [15] J. Burke,[16,17] Y.-Z. Cai [18] T.-W. Chen,[19] P. Chen,[20] R. Ciolfi [2,21] S. Dong,[20] S. Gomez,[22] M. Gromadzki [23] C. P. Gutiérrez [24,25] D. Hiramatsu,[16,17,26,27] G. Hosseinzadeh,[28] D. A. Howell,[16,17] A. Jerkstrand,[19] E. Kankare,[29] A. Kozyreva [30] K. Maguire [31] C. McCully,[16] P. Ochner,[2,32] C. Pellegrino,[16,17] G. Pignata,[5,6] R. S. Post,[33] N. Elias-Rosa,[2,34] M. Shahbandeh,[35] S. Schuldt,[30,36] B. P. Thomas,[37] L. Tomasella [2] J. Vinkó,[37,38,39,40] C. Vogl,[30] J. C. Wheeler [37] and D. R. Young[41]

Affiliations are listed at the end of the paper

Accepted 2022 March 14. Received 2022 March 14; in original form 2021 November 9

ABSTRACT

SN 2018hti was a very nearby ($z = 0.0614$) superluminous supernova with an exceedingly bright absolute magnitude of -21.7 mag in r band at maximum. The densely sampled pre-maximum light curves of SN 2018hti show a slow luminosity evolution and constrain the rise time to $\sim$50 rest-frame d. We fitted synthetic light curves to the photometry to infer the physical parameters of the explosion of SN 2018hti for both the magnetar and the CSM-interaction scenarios. We conclude that one of two mechanisms could be powering the luminosity of SN 2018hti; interaction with $\sim$10 $M_\odot$ of circumstellar material or a magnetar with a magnetic field of $B_p \sim 1.3 \times 10^{13}$ G, and initial period of $P_{spin} \sim 1.8$ ms. From the nebular spectrum modelling we infer that SN 2018hti likely results from the explosion of a $\sim$40 $M_\odot$ progenitor star.

Key words: supernovae: general – supernovae: individual: SN 2018hti.

1 INTRODUCTION

It is widely accepted that the explosion of massive stars ($\gtrsim$8 $M_\odot$, e.g. Smartt 2009) is triggered by the gravitational collapse of their cores. This leads to a core-collapse supernova (SN) explosion, whose light curves (LCs) reach an absolute magnitude at maximum usually ranging between -14 and -19 mag (e.g. Richardson et al. 2014; Modjaz, Gutiérrez & Arcavi 2019) in optical bands. These luminosities are suitably explained with the decay of <0.1 $M_\odot$ of ^{56}Ni (e.g. Nadyozhin 1994; Müller et al. 2017; Anderson 2019; Prentice et al. 2019) and with the thermal energy deposited in the progenitor's envelope during the gravitational collapse. The discoveries of superluminous supernovae (SLSNe) with an absolute magnitude even brighter than -21 mag (e.g. Gal-Yam 2012, 2019a; Howell 2017) challenge this standard SN paradigm. In fact, $\gtrsim$5 $M_\odot$ of ^{56}Ni would be required to account for these luminosities (e.g. Kasen, Woosley & Heger 2011; Dessart et al. 2012).

Apart from their exceptional brightness, SLSNe are characterized by their pre-maximum/maximum optical spectra, usually showing a hot ($\gtrsim$15 000 K) continuum. Similar to the classical SNe (Minkowski 1941), SLSNe are subclassified as SLSNe I and SLSNe II depending on whether they are hydrogen deficient or hydrogen rich, respectively (Gal-Yam 2012). In addition, SLSNe IIn are characterized by the presence of multicomponent/narrow Balmer emission lines in their spectra and most likely fill the high-luminosity tail of the luminosity function of SNe IIn (Gal-Yam 2012).

SLSNe I are usually discovered in metal-poor and star-forming host galaxies (Chen et al. 2013, 2017a; Lunnan et al. 2014; Leloudas et al. 2015; Perley et al. 2015; Schulze et al. 2018). They are recognized by the presence of prominent absorptions between 3000 and 5000 Å in their pre-maximum/maximum optical spectra. This is an almost unique feature of SLSNe I, usually identified as the contribution of O II transitions (e.g. Quimby et al. 2011; Mazzali et al. 2016; Gal-Yam 2019b), although this identification has been questioned (e.g. Könyves-Tóth & Vinkó 2020). However, these features were observed also in the SN Ib SN 2008D (Soderberg et al. 2008), and in the recently proposed SN subclass of SNe Icn (Gal-Yam et al. 2021; Pastorello et al. 2021) and in the Type-II SN 2019hcc (Parrag et al. 2021). 15–20 d after maximum luminosity, the spectra of SLSNe I start to remarkably reproduce the behaviour of SNe Ic and SNe Ic broad lined (SNe Ic BL) at maximum luminosity (e.g. Pastorello et al. 2010). Interestingly, recent discoveries of SLSNe I and SNe Ic appear to fill the luminosity gap between these two subclasses (such as the cases of the luminous SNe Ic SN 2012aa, SN 2019stc, Roy et al. 2016, Gomez et al. 2021). The physical explanation linking these SN subclasses is still a matter of investigations (e.g. Zou & Cheng 2018; Blanchard et al. 2019; Lin et al. 2020b). The photometric evolution of SLSNe I is more heterogeneous: LCs of SLSNe I typically evolve either smoothly (e.g. SN 2010gx, SN 2011ke, Pastorello et al. 2010; Inserra et al. 2013) or they can show a complex behaviour with pre-/post-maximum bumps (e.g. SN 2015bn, iPTF15esb, SN 2017gci, SN 2018don, Nicholl et al. 2015b; Yan et al. 2015; Angus et al. 2019; Lunnan et al. 2020; Fiore et al. 2021, see also Hosseinzadeh et al. 2021). Their LCs evolve over a very broad range of time-scales; a diversity which prompted

★ E-mail: achillefiore@gmail.com (AF); stefano.benetti@inaf.it (SB)

© 2022 The Author(s)
Published by Oxford University Press on behalf of Royal Astronomical Society

Downloaded from https://academic.oup.com/mnras/article/512/3/4484/6549929 by Biblioteca Dipartimento di Scienze Economiche user on 06 February 2023

the community to propose a slow/fast-evolving subclassification of SLSNe I events, but the discovery of intermediate objects (e.g. Gaia16apd, SN 2017gci, Kangas et al. 2017; Nicholl et al. 2017a; Yan et al. 2017a; Fiore et al. 2021; Stevance & Eldridge 2021) and statistical studies (Nicholl et al. 2015a; De Cia et al. 2018; Lunnan et al. 2018b; Angus et al. 2019) point towards a continuous distribution between the two subcategories.

There is no general consensus about the engine powering SLSNe (see Moriya, Sorokina & Chevalier 2018, for a recent review). Several scenarios have been proposed to explain the huge luminosities of SLSNe I: (i) the magnetar scenario, which considers the contribution of the radiation-dominated wind inflated by a spinning down millisecond magnetar (e.g. Kasen & Bildsten 2010; Woosley 2010; Inserra et al. 2013; Chen et al. 2015, 2017b; Wang et al. 2015; Chen, Woosley & Sukhbold 2016; Nicholl, Guillochon & Berger 2017b; Margalit et al. 2018; Vurm & Metzger 2021); (ii) the interaction of the SN ejecta with shells of circumstellar material (CSM, e.g. Chevalier & Fransson 2003; Chevalier & Irwin 2011; Ginzburg & Balberg 2012; Chatzopoulos et al. 2013; Nicholl et al. 2014, 2020; Smith 2017; Lunnan et al. 2018a, 2020) lost by the progenitor star prior to its explosion via stellar winds or alternatively via the pulsational-pair instability phenomenon (e.g. Woosley, Blinnikov & Heger 2007; Woosley 2017; Renzo et al. 2020); (iii) the pair-instability scenario, where e^+, e^- pair creation in a very massive star (with a He-core mass $64\,\mathrm{M}_\odot \lesssim M_{\rm He} \lesssim 133\,\mathrm{M}_\odot$, e.g. Heger & Woosley 2002) induces the collapse of the star and triggers a thermonuclear runaway in the core, allowing for a massive production of ^{56}Ni. CSM interaction is usually invoked as the major power source for (SL)SNe IIn (as in the case of SN 2006gy, Smith & McCray 2007; Smith et al. 2007; Agnoletto et al. 2009) as it provides a suitable explanation for the narrow/multicomponent features usually seen in their spectra. SLSNe I LCs can be reasonably well explained by CSM models too (e.g. Chevalier & Fransson 2003; Chevalier & Irwin 2011; Ginzburg & Balberg 2012; Chatzopoulos et al. 2013), although the SLSNe I spectra lack for strong interaction signatures. However, it has been shown (Chevalier & Irwin 2011; Moriya & Tominaga 2012; Smith et al. 2015; Andrews & Smith 2018; Bhirombhakdi et al. 2019) that a buried CSM interaction might suppress these features under specific conditions, e.g. if the SN progenitor star is surrounded by a CSM disc (Smith 2017). The complexities in some SLSNe LCs are also indicative of CSM interaction. While the simplest explanation for these complexities is late-time interaction with shells or clumps of CSM (e.g. Moriya et al. 2018), Metzger et al. (2014) argue that they can be mimicked by the opacity variations due to wind-driven ionization fronts of a millisecond magnetar.

In this work, we present and discuss the spectrophotometric observations of SLSN I SN 2018hti, located at RA $= 03^{\rm h}\,40^{\rm m}\,53.76^{\rm s}$, Dec. $= +11^\circ\,46'37.17''$. SN 2018hti was discovered on 2018 November 1 by the Asteroid Terrestrial-impact Last Alert System (ATLAS) project (Tonry et al. 2018a,b) and initially named ATLAS18yff. It was then classified on 2018 November 6 by Burke et al. (2018) as an SLSN I. Independent spectrophotometric data of SN 2018hti are already presented by Lin et al. (2020a) and imaging polarimetry data of SN 2018hti are presented by Lee (2019). Here, we present the photometric and spectroscopic data of SN 2018hti in Sections 2 and 3, respectively. We discuss in Section 4 the spectrophotometric data of SN 2018hti: in particular, the metallicity measurements of its host galaxy (Section 4.1), the blackbody temperature and radius evolutions (Section 4.2), the photospheric velocity (Section 4.3), some photometric and spectroscopic comparisons of SN 2018hti with a selected sample of SLSNe I (Section 4.4), and finally the suitability of magnetar and of CSM-interaction scenarios for SN 2018hti (Section 4.5).

In the following sections, we will assume a flat Universe with $H_0 = 71 \pm 3\,\mathrm{km\,s^{-1}\,Mpc^{-1}}$, $\Omega_\Lambda = 0.69$, $\Omega_{\rm M} = 0.31$ (taking an average of H_0 among the estimates provided by Planck Collaboration XIII 2016; Khetan et al. 2021; Riess et al. 2021). Hence, the redshift $z = 0.0614$ (see Section 3) measured with the narrow emission lines from the host galaxy corresponds to a luminosity distance $d_{\rm L} = 271.2^{+12}_{-11}$ Mpc.

2 PHOTOMETRY

2.1 Observations and data reduction

We led the multiband photometric follow-up of SN 2018hti via several facilities. Ultraviolet (*uvw*2, *uvm*2, *uvw*1) and *U*, *B*, *V* imaging was obtained with the *Neil Gehrels Swift* Observatory+UVOT (Gehrels et al. 2004). Optical/near-infrared (NIR) *u*, *B*, *g*, *V*, *r*, *i*, *z*, *J*, *H*, $K_{\rm s}$ photometric follow-up was obtained via the NOT Unbiased Transient Survey[1] (NUTS/NUTS2, Mattila et al. 2016; Holmbo et al. 2019) at the 2.56-m Nordic Optical Telescope (NOT)+ALFOSC/NOTCam at the Roque de los Muchachos Observatory, La Palma (Spain), the 1.82m Copernico Telescope+AFOSC and Schmidt Telescopes at the Asiago Astrophysical Observatory (Italy), the 1.2 m telescope at the Fred Lawrence Whipple Observatory+KeplerCam and the 0.6/0.8-m telescopes at the Post Observatory (CA, USA), and Post Observatory Mayhill (NM, USA). We also include the the Asteroid Terrestrial-impact Last Alert System (ATLAS)-photometry, the early ZTF public photometry available via the IRSA[2] archive and Las Cumbres Observatory (LCO)-network[3] *U*, *B*, *g*, *V*, *r*, *i* photometry. LCO data (Brown et al. 2013) come from the Global Supernova Project. ATLAS- *o* and *c* magnitudes were converted to standard Sloan *g* and *r* filter following Tonry et al. (2018a, cfr. equation 2 therein) and Tonry et al. (2012, cfr. equation 6 and table 6 therein). As the colour transformations used within these equations are determined from a stellar spectral energy distribution (SED), the conversion tends to increase the uncertainty of the resulting magnitudes. Also, at very early epochs the $g - r$ colour was estimated via a colour extrapolation since the coeval *g*, *r*-filter photometry is not available. Lastly, we included the mid-infrared (MIR) photometry observed with the Wide-field Infrared Survey Explorer (WISE) NASA mission in the *W*1 and *W*2 wavelength bands.

Photometry was performed with the ECSNOOPY package[4] (Cappellaro 2014) using the point spread function (PSF) fitting technique. A detailed description of the image-processing procedures can be found in Fiore et al. (2021). In particular, for SN 2018hti we removed the background contamination using the template-subtraction technique in the *u*-, *U*-, *B*-, *g*-, *V*-, *r*-, *i*-, *z*-, *W*1-, *W*2-filter images. This was performed with ECSNOOPY via HOTPANTS (Becker 2015). Suitable deep template *u*-, *U*-, *B*-, *V*-filter frames were obtained at the NOT via NUTS2 on 2020 February 25, namely 414 rest-frame days after maximum light and we used PanSTARRS *g*, *r*, *i*, *z* pre-explosion images as template frames. We assumed that SN 2018hti already faded well below the detection limit and used these frames as templates. The

[1] http://nuts2.sn.ie.
[2] https://irsa.ipac.caltech.edu/.
[3] https://lco.global/.
[4] ECSNOOPY is a package for SN photometry using PSF fitting and/or template subtraction developed by E. Cappellaro. A package description can be found at http://sngroup.oapd.inaf.it/ecsnoopy.html.

Downloaded from https://academic.oup.com/mnras/article/512/3/4484/6549929 by Biblioteca Dipartimento di Scienze Economiche user on 06 February 2023

*W*1, *W*2 frames used as template frames for the WISE photometry were obtained by the WISE mission on 2018 August 18, 19 (MJD = 58348.35, 58349.47), i.e. before the explosion of SN 2018hti. For the NIR frames, the background level was interpolated with a low-order polynomial since no suitable deep template frame in *J*, *H*, K_s band was available. *B*, *g*, *V*, *r*, *i*, *z* magnitudes were calibrated having evaluated the photometric zero-points and colour terms with a sequence of field stars from the Pan-STARRS (Panoramic Survey Telescope and Rapid Response System, Chambers et al. 2016) catalogue. The WISE magnitudes were calibrated with their instrumental zero-points. Calibrated PanSTARRS magnitudes were converted to standard SDSS system following Tonry et al. (2012, see equation 6). *u* magnitudes could not be calibrated with the SDSS survey as SN 2018hti was located outside of its sky coverage. Hence, we calibrated the *u* magnitudes of the local field stars against *u*-band photometry of Sloan standards fields taken on the same photometric night. For *U*, *B*, *V* images the calibration was done after converting the Pan-STARRS magnitudes to Sloan magnitudes as before, and then from Sloan magnitudes to Johnson system following Chonis & Gaskell (2008). NIR magnitudes were calibrated with a local sequence of stars from the Two-Micron All Sky Survey (Skrutskie et al. 2006). *Swift*/UVOT *uvw*2-, *uvm*2-, *uvw*1-, *U*-, *B*-, *V*-filter magnitudes were measured by stacking the layers of the individual observing segments with the task UVOTIMSUM. We then measured the brightness using a 2 arcsec-radius aperture with the task UVOTSOURCE task in HEASOFT version 6.25 ((HEASARC) 2014). To calibrate the *Swift*/UVOT magnitudes, we used the recently updated version (2020 November) of the sensitivity corrections. We also analysed data from the *Swift* X-ray telescope by first stacking all 29 UVOT exposures. The total amount of observing time amounts to 52.3 ks. No source was detected at the location of SN 2018hti. The $3\,\sigma$ upper limit on the 0.3–10 keV count rate at the SN position is 6.6×10^{-4} counts s^{-1}. Assuming a power-law X-ray spectrum and the Galactic column density of 1.6×10^{21} cm^{-2} and the distance given in Section 1, we derive an upper limit on the 0.3–10 keV unabsorbed luminosity of 4×10^{41} erg s^{-1}. This is the maximum mean luminosity the SN could have had during the entire *Swift* campaign. Under the hypothesis that the putative X-ray emission follows the UV emission, we restricted our analysis to a time interval centred on the UV peak time in a ±6 d around maximum. We selected five observations for a total exposure time of 7.9 ks. The SN is still undetected with a $3\,\sigma$ upper limit on the 0.3–10 keV count rate of 4.7×10^{-3} counts s^{-1}, corresponding to a 0.3–10 keV unabsorbed luminosity of 3×10^{42} erg s^{-1}.

Each instrument used for the observational follow-up has its own instrumental throughput. This difference introduces systematic errors when magnitudes are obtained with multiple instruments. To account for this effect, we compute the *B*, *V*, *g*, *r*, *i* S-corrections (Stritzinger et al. 2002) for each instrumental configuration using the observed optical spectra of SN 2018hti (similar to Pignata et al. 2004; Elias-Rosa et al. 2006; Fiore et al. 2021) and propagated this into the calculation of the pseudo-bolometric LC. However, we noticed that this correction does not affect our analysis.

The resulting S-correction for the *B*, *V*, *g*, *r*, *i* filters and for each instrumental set-up is shown in Fig. 1. For the *u*, *U*, *z*, *J*, *H*, K_s filters (which are not covered by the observed optical/NIR spectra), we repeated the above procedure for a set of blackbody spectra shifted to the observer frame of SN 2018hti. The blackbody spectra have temperatures spanning a range of 8000–25 000 K which broadly agrees with the best-fitting blackbody temperatures of the spectra of SN 2018hti (see Section 4.2). In this way, the S-corrections computed for the blackbody spectra provide an estimate of the S-correction outside the optical range. Unfortunately, this approach does not account for the presence of broad emission lines in the SN spectrum, which may alter the estimate of the S-correction. Synthetic-photometry measurements on the two available UV/NIR maximum/post-maximum spectra of other SLSNe I (Gaia16apd, Kangas et al. 2017, and an NIR spectrum of the SN Ic BL SN 1998bw) show that the S-corrections computed on the spectra agree with those computed on their blackbody fit within ∼0.05 mag for the *z*, *J*, *H*, K_s filters. In the *u* and *U* bands, the blackbody approximation overcorrects the magnitudes with respect to the spectra of Gaia16apd (probably due to the line blanketing). This is true also for the NOTCam S-corrections calculated on the NIR IRTF+SpeX spectrum. To carefully account for this effect requires a denser and better-sampled spectroscopic follow-up outside the optical range, which at the moment has not been done for SLSNe. We therefore opted for the conservative approach of propagating the maximum S-correction ΔS_{corr} computed for the blackbody fits into the error of the pseudo-bolometric LC calculation (see Section 2.3).

The reduced *uvw*2, *uvm*2, *uvw*1, *u*, *U*, *B*, *g*, *V*, *r*, *i*, *z*, *J*, *H*, K_s, *W*1, *W*2 magnitudes are reported in Tables A1– A5. The S-corrections S_{corr} and the ΔS_{corr} values are listed in Tables A6–A10.

2.2 K-corrections

We computed the *K*-corrections of SN 2018hti for the *B*-, *V*-, *g*-, *r*-, *i*-filter magnitudes performing synthetic photometry measurements on to the observed-frame ($m_{s,\,obs}$) and rest-frame ($m_{s,\,rest}$) optical spectra (see Section 3). These were performed with the PYSYNPHOT PYTHON package.[5] For each filter and each spectrum, the *K*-corrections were computed as $K = m_{s,\,obs} - m_{s,\,rest}$ and are listed in Table A11. The measured *K*-corrections are linearly interpolated to the epochs of the imaging observation and subsequently subtracted from the magnitudes of SN 2018hti as measured on those images. *uvw*2, *uwm*2, *uvw*1, *u*, *U*, *z*, *J*, *H*, K_s *K*-corrections were estimated using the SED blackbody fits in place of the observed spectra.

2.3 Observed and pseudo-bolometric LCs

The UV-optical-NIR observed LCs of SN 2018hti are shown in Fig. 2 and are plotted against the phase corrected for time dilation. To estimate the maximum luminosity epoch, we fit a fourth-order polynomial to the *r*-band LC and infer a magnitude at maximum $r_{max} \simeq 16.5 \pm 0.2$ mag at MJD = 58 464.5 ± 4.0 (in agreement with the maximum found by Lin et al. 2020a). Given a distance modulus $\mu = 37.17 \pm 0.1$ mag and a Galactic extinction[6] $A_V = 1.280$ mag (Schlafly & Finkbeiner 2011), assuming the extinction law $A_V = 3.1 \times E(B - V)$ (Cardelli, Clayton & Mathis 1988, 1989), the absolute peak *r*-filter magnitude is $M_r = -21.7 \pm 0.2$ mag. We assume no internal extinction from the host galaxy, supported by the absence of the interstellar Na ID doublet and by the fact that the Hα/Hβ ratio remains similar to the expected value for case-B recombination (Groves, Brinchmann & Walcher 2012).

The earliest ATLAS detection was obtained on 2018 October 22 (MJD = 58 413.54) and the last ATLAS detection limit was exactly 3 d before (MJD = 58 410.54). If we assume that the latter is a genuine non-detection, this provides an estimate of the explosion epoch of

[5]https://pysynphot.readthedocs.io/.
[6]Obtained via the NASA/IPAC Extragalactic Database https://ned.ipac.caltech.edu/extinction_calculator.

Downloaded from https://academic.oup.com/mnras/article/512/3/4484/6549929 by Biblioteca Dipartimento di Scienze Economiche user on 06 February 2023

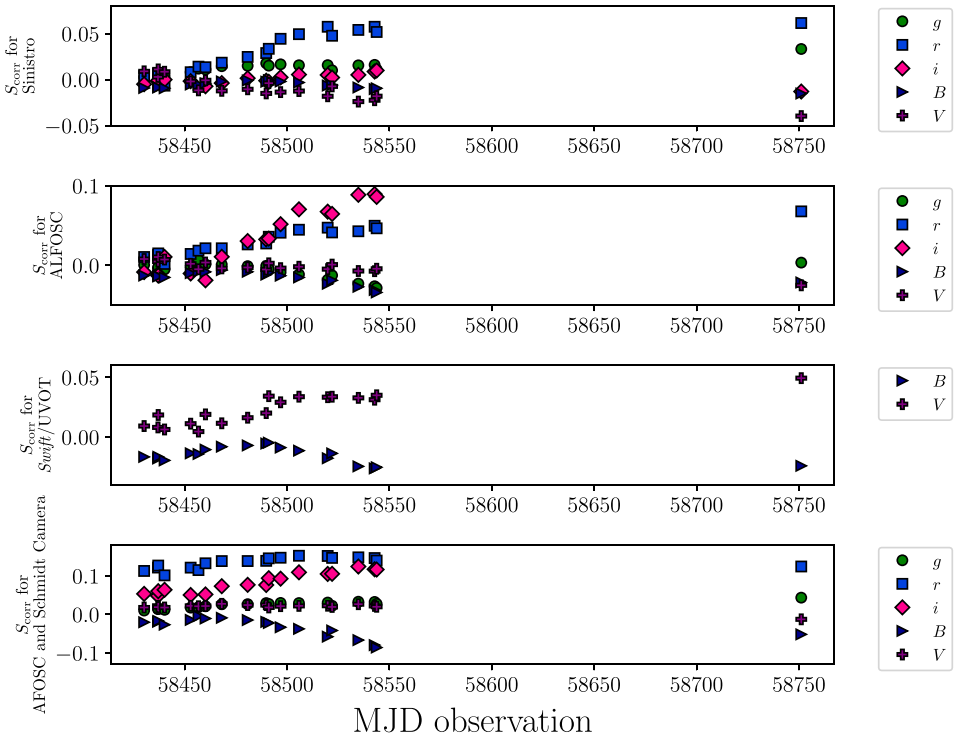


Figure 1. S-correction in *B*-, *V*-, *g*-, *r*-, and *i*-filter passbands for different instruments (Sinistro, ALFOSC, *Swift*/UVOT, AFOSC/Schmidt Camera, in descending order).

MJD = 58 412.04 ± 1.5. With this, the maximum-luminosity epoch implies a rest-frame rise time of $\tau_{\rm rise} = 50 \pm 6$ d, which is typical of the slow-evolving SLSNe I (Inserra 2019). Finally, after ∼100 d from maximum light, SN 2018hti disappeared behind the Sun. For each filter, the LC evolution is characterized by a relatively slow rise to maximum and a post-maximum decline rate of ∼1–2 × $\tau_{\rm rise}$ in each filter. Moreover, the *r*-filter LC apparently shows a levelled off start at earliest phases, which is hard to reconcile with the overall trend of the LC. However, as noticeable in Fig. 2, the very early detections in *r* filter were retrieved by the *o*-filter ATLAS magnitudes whose colour transformations is uncertain. For this reason we also show the observed ATLAS *o*-filter LC in Fig. 3 (top panel), which presents a similar slope change for the first point. To quantify the deviation of the first ATLAS detection from the early behaviour of the LC, we fit a parabola to the ATLAS flux density (expressed in μJy) assuming a flux scaling $F \propto t^2$ (e.g. Riess et al. 1999; Conley et al. 2006). Under this assumption, the first ATLAS point is ∼0.7 mag brighter than the predicted LC. However, the early *r*- and ATLAS *o*-filter detection limits (see Figs 2 and 3) exclude the occurrence of a pre-maximum bump (as in Leloudas et al. 2012; Nicholl et al. 2015b; Smith et al. 2016) up to ∼53 rest-frame days before the estimated explosion epoch. However, we note that the post-maximum epochs ATLAS *o*-filter data fluctuate within ∼0.25 mag in a time-scale ≲10 d. This allows for a 0.25 mag maximum uncertainty for ATLAS magnitudes, which is much less than the 0.7 mag deviation for the first point, making the flat start more credible. Finally, the *K*-corrected and S-corrected *uvw*2, *uvm*2, *uvw*1, *u*, *U*, *B*, *g*, *V*, *r*, *i*, *z*, *J*, *H*, $K_{\rm s}$, *W*1, *W*2 host-template subtracted photometry of SN 2018hti was combined to obtain the pseudo-bolometric LC displayed in Fig. 4 (data are listed in Table A12). This was computed by integrating the multiband photometry neglecting every flux contribution out of the integration boundaries. For SN 2018hti, the epochs of the *r*-band photometry are adopted as reference. The extinction-corrected combined fluxes were finally converted to pseudo-bolometric luminosities by multiplying by $4\pi d_{\rm L}^2$. Similar to the multiband LCs, the pseudo-bolometric LC has a ratio $\tau_{\rm decline}/\tau_{\rm rise} \sim 1.8$ (similar to other SLSNe I, see e.g. Nicholl et al. 2015a).

3 SPECTROSCOPY

3.1 Observations and data reduction

We collected a dense sample of spectra for SN 2018hti starting from MJD = 58 430.2 (2018 November 8), which corresponds to 32 rest-frame days before maximum light.

We led the spectroscopic follow-up via the extended/advanced Public ESO Spectroscopic Survey for Transient Objects (Smartt et al. 2015) (ePESSTO/ePESSTO+), NUTS/NUTS2, with the 1.82-m Copernico telescope at the Asiago astrophysical observatory, Italy, the 2.4m Hiltner Telescope+OSMOS (Ohio State Multi-Object Spectrograph) at the Michigan-Dartmouth-MIT Observatory, and the Hobby Eberly Telescope (HET)+LRS2 (Low Resolution Spectrograph) at the McDonald observatory, Texas. Moreover, we took a pre-maximum (−18 rest-frame days) NIR spectrum via the 3.0-m NASA Infrared Telescope Facility (IRTF)+SpeX (Rayner et al. 2003) and a nebular spectrum on 2019 September 24 (+269 rest-frame days) with the 10.4m Gran Telescopio CANARIAS (GTC)+OSIRIS (Optical System for Imaging and low-Intermediate-Resolution Integrated Spectroscopy, Cepa et al. 2000) at Roque de los Muchachos Observatory. Additional FLOYDS spectra were obtained from FLOYDS on the Faulkes Telescope South (or North) as part of the Global Supernova Project. The instrumental set-ups

Downloaded from https://academic.oup.com/mnras/article/512/3/4484/6549929 by Biblioteca Dipartimento di Scienze Economiche user on 06 February 2023

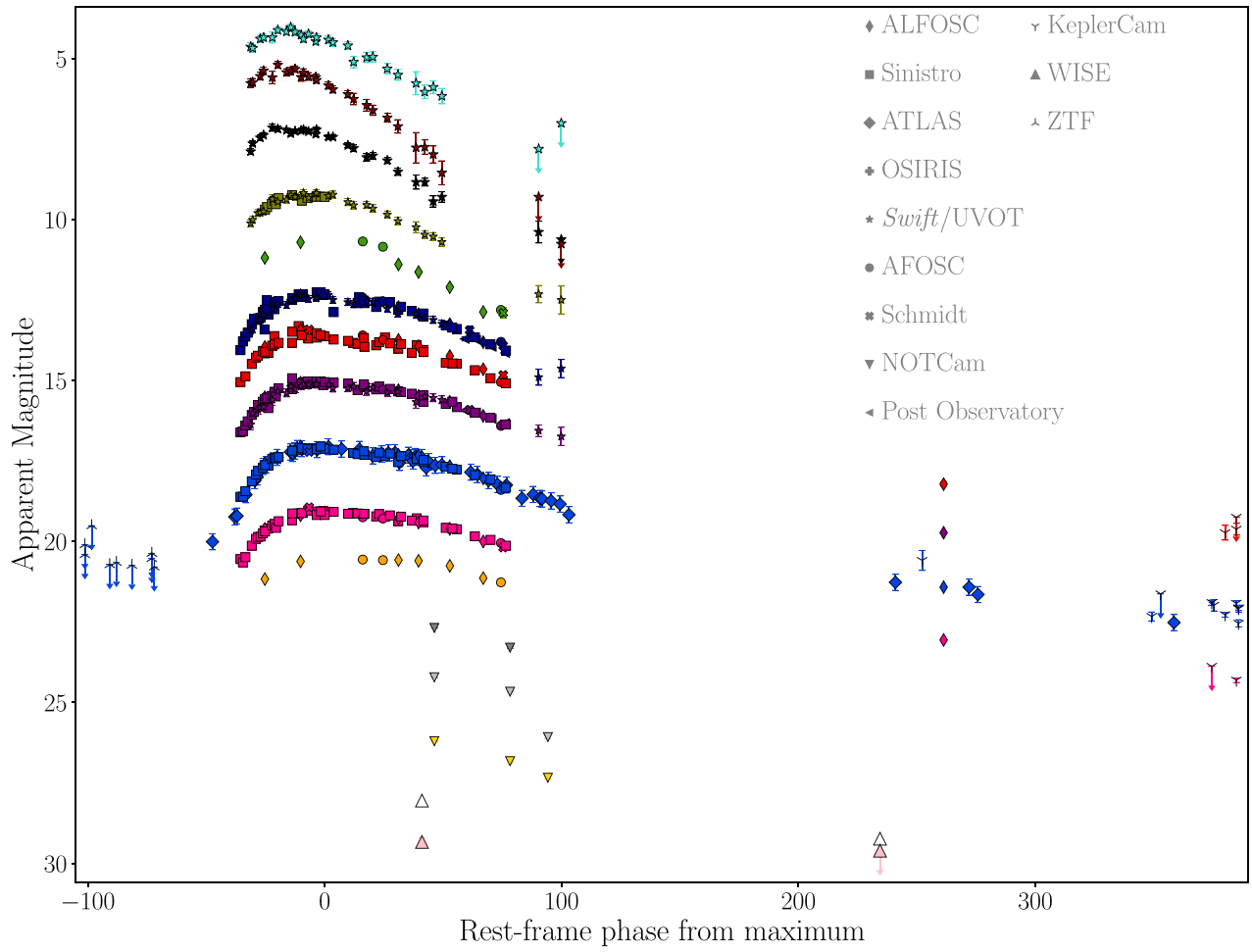


Figure 2. *uvw*2, *uvm*2, *uvw*1, *U*, *u*, *B*, *g*, *V*, *r*, *i*, *z*, *J*, *H*, K_s, *W*1, *W*2 observed LCs of SN 2018hti, respectively, plotted in brown, cyan, black, dark green, dark blue, green, blue, red, purple, magenta, orange, silver, yellow, white, and pink. Data obtained with different instruments are plotted with different markers, as labelled in the top-right corner. Magnitudes are plotted in ABmags.

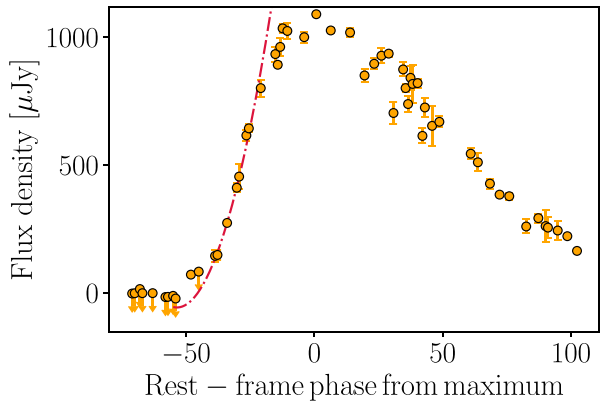


Figure 3. ATLAS-*o* LCs of SN 2018hti (yellow dots) in flux space (expressed in μJy). The early ATLAS LC is fitted with a second-order polynomial (dash–dotted red line).

and the resolution of the spectra presented in this work are listed in Table A13.

The AFOSC, EFOSC2, and GTC spectra were reduced with the standard IRAF procedures. First, the raw bidimensional spectroscopic frames were debiased, flatfielded, and corrected for the cosmic rays contribution with the Laplacian Cosmic Ray Identification package (LACOSMIC, van Dokkum 2001). Then the spectra were extracted along the spatial direction with the IRAF task APALL after having subtracted the background contribution, which was estimated via a low-order polynomial fit. The one-dimensional spectra were wavelength-calibrated against HeAr (for the NTT+EFOSC2), HeNe (for NOT+ALFOSC spectra), NeHgCd (for the 1.82m-Copernico+AFOSC spectra), and HgArNe (for GTC+OSIRIS spectrum) calibration arcs. Then the extracted one-dimensional spectra were flux calibrated via a set of spectrophotometric standard stars observed on the same night and with the same instrumental set-up as the science observations. Using the flux-calibrated standard star spectrum we were able to remove the contribution of the telluric absorption features. Finally, the flux calibration was checked against coeval photometry. The ALFOSC spectra were reduced with

Downloaded from https://academic.oup.com/mnras/article/512/3/4484/6549929 by Biblioteca Dipartimento di Scienze Economiche user on 06 February 2023

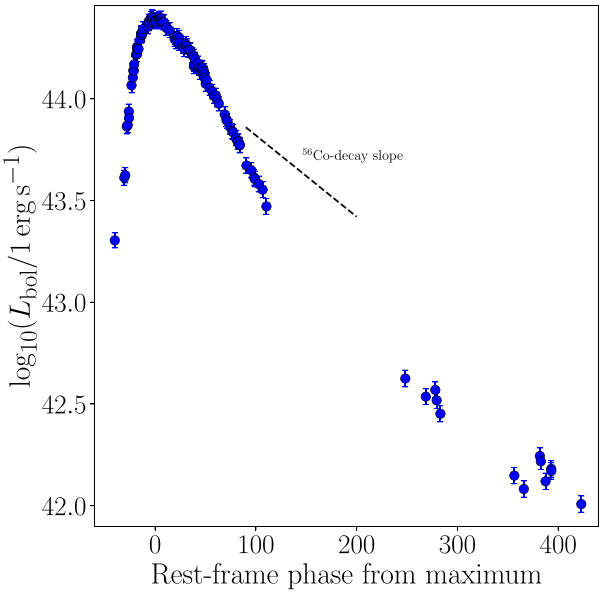


Figure 4. Pseudo-bolometric LC of SN 2018hti (blue dots). The black dashed line indicates the slope of ^{56}Co-decay.

FOSCGUI.[7] The OSMOS spectrum was reduced with the PYRAF-based SIMSPEC[8] pipeline. The LRS2 spectra were reduced with a dedicated IRAF- and PYTHON-based pipeline (as in Yang et al. 2020, see section 2.2.3). FLOYDS spectra were reduced using the FLOYDSSPEC pipeline[9]. The IRTF+SpeX spectrum was reduced utilizing the SPEXTOOL software package (Cushing, Vacca & Rayner 2004).

3.2 Spectral evolution and line identifications

The spectral evolution of SN 2018hti is shown in Fig. 5. Throughout their evolution, the spectra of SN 2018hti show Hβ, Hα, [O III] λ 4959, [O III] λ 5007 narrow emission lines from the host galaxy, which we used to measure the redshift of the host galaxy and to estimate the metallicity at the site of SN 2018hti (see Section 4.1).

The pre-maximum/maximum-light spectra of SN 2018hti present a very hot continuum reaching blackbody temperatures of $\sim$18 000$-$22 000 K. They show the W-shaped O II absorptions between 3500 and 5000 Å. In addition, from the earliest spectrum at phase $-$34 d from the maximum light, a broad feature (FWHM$\sim$15 000–18 000 km s^{-1}) starts to rise in a nearly boxy fashion (see Section 4.5.1). We interpreted this feature as C II λ 6580 (as in Nicholl et al. 2014, see also the discussion in Section 4.5.1). We also mention that the TARDIS modelling of a sample of more than 180 spectra of SLSNe I predicts a C II 6584.70 at a fraction above 50 per cent with a small contribution of Ne I $\lambda\lambda$ 6404.02, 6508.83 (Paraskeva et al. in preparation). This feature does not however reproduce a boxy profile. The early NIR spectrum of SN 2018hti (see Fig. 6) shows an almost featureless continuum with the exception of an emission at a rest-frame wavelength about $\simeq$ 9200 Å which we interpreted as C II λ 9234, similar to the cases of Gaia16apd (Yan et al. 2017a) and to SN 2015bn (Nicholl et al. 2016).

In the spectrum taken 4 d after maximum light, the Fe II emission features are visible in the blue regions, while Mg II begins to be seen in the 15 d post-maximum spectrum. On the same epoch, O I λ 7774 appears in the red end of the spectrum. About 15–30 d after maximum light, the spectrum of SN 2018hti smoothly enters the SN Ic/SNe Ic BL-like phase, similarly to many other SLSNe I (e.g. Pastorello et al. 2010; Inserra et al. 2013; Gal-Yam 2019a). After 39 rest-frame days from maximum an emission shows up at $\sim$6360 Å, which we interpreted as Si II λ 6355. In the 52 d post-maximum spectrum the Ca II NIR $\lambda\lambda\lambda$ 8498, 8542, 8662 triplet becomes visible. After SN 2018hti reappeared from behind the sun, we took the GTC+OSIRIS spectrum on 2019 September 24, 269 d after maximum light. This spectrum is not completely nebular as it displays some residual continuum, which could be however influenced by a residual contribution from the host galaxy (see also Jerkstrand et al. 2017). This phase was referred to as 'pseudo-nebular' by Nicholl et al. (2019).

4 DISCUSSION

Here, we discuss the data presented above. Where possible, we compare data of SN 2018hti with those of other SLSNe I. To do this, we selected a sample of SLSNe I which share some spectrophotometric properties with those of SN 2018hti. We included LSQ14bdq (Nicholl et al. 2015b), SN 2006oz (Leloudas et al. 2012), and DES14X3taz (Smith et al. 2016) since their *r*-filter LCs show a pre-maximum bump. Moreover, SN 2015bn (Nicholl et al. 2016) was prompted as the best-spectral match by GELATO (Harutyunyan et al. 2008). The SLSNe I iPTF13ehe, iPTF15esb, and iPTF16bad (Yan et al. 2015, 2017b) were added to the comparison sample since they show Hα, although at later epochs with respect to maximum light. Finally, we added also a late spectrum of Gaia16apd (Kangas et al. 2017) since few SLSNe I spectra are available at pseudo-nebular/nebular phases.

4.1 Metallicity at the location of SN 2018hti

As mentioned earlier, SLSNe I usually explode in metal-poor, star-forming environments. Several metallicity diagnostics are calibrated from the emission lines emerging from the host-galaxy spectrum. In the case of SN 2018hti, we measured the flux emitted by the [O II] λ 3727, Hβ, [O III] λ 4959, [O III] λ 5007, Hα, and [S II] λ 6717 narrow emission lines emerging from the host galaxy in the nebular spectrum. To measure the flux emitted within the narrow emission lines, we extracted the host-galaxy spectrum close to the position of SN 2018hti by placing the aperture adjacent to the SN itself.

One of these indicators is referred to as R_{23} (Pagel et al. 1979):

$$R_{23} = \frac{([\mathrm{O\,II}]\lambda\,3727 + [\mathrm{O\,III}]\lambda\,4959, 5007)}{\mathrm{H}\beta}. \quad (1)$$

Another indicator which is often used is the so-called N2O2 (Kewley & Dopita 2002):

$$\mathrm{N2O2} = \frac{[\mathrm{N\,II}]\lambda\,6584}{[\mathrm{O\,II}]\lambda\,3727}. \quad (2)$$

For SN 2018hti, we found $\log_{10}R_{23} = 0.96$ and $\log_{10}(\mathrm{N2O2}) = -1.26$. To measure the metallicity of the host galaxy at the site of SN 2018hti, we evaluated different metallicity estimators

[7] FOSCGUI is a graphic user interface aimed at extracting SN spectroscopy and photometry obtained with FOSC-like instruments. It was developed by E. Cappellaro. A package description can be found at http://sngroup.oapd.inaf.it/foscgui.html.
[8] https://astro.subhashbose.com/simspec/.
[9] https://github.com/svalenti/FLOYDS_pipeline/blob/master/bin/floydsspec/

Downloaded from https://academic.oup.com/mnras/article/512/3/4484/6549929 by Biblioteca Dipartimento di Scienze Economiche user on 06 February 2023

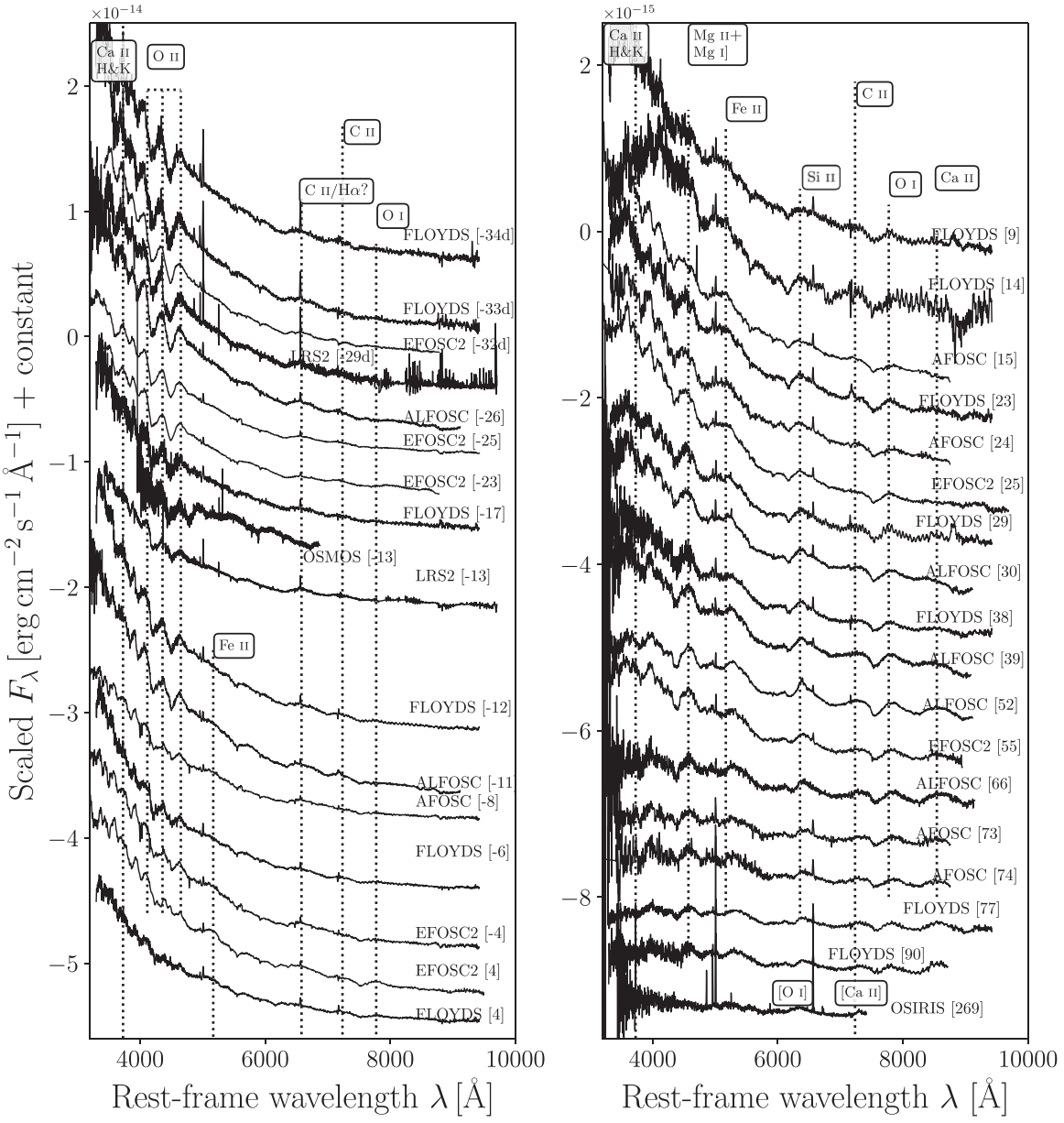


Figure 5. Spectral evolution of SN 2018hti. Spectral line identifications are marked with vertical black dotted lines, and labelled on its right side with the corresponding ion. The rest-frame phase with respect to maximum luminosity is reported on the right side of each spectrum. The left-hand panel shows the spectral evolution of SN 2018hti from −34 to 4 d from maximum luminosity and the right-hand panel shows the remaining spectra up to 269 d after maximum luminosity.

simultaneously due to the tool PYMCZ[10] presented by Bianco et al. (2016). PYMCZ randomly samples a Gaussian distribution whose mean and standard deviation are given by the flux measurements and their uncertainties, respectively. With this tool, it was possible to exploit the D04 (Denicoló, Terlevich & Terlevich 2002), M91 (McGaugh 1991), M08_N2HA, M08_O3O2 (Maiolino et al. 2008), and M13_N2 (Marino et al. 2013) metallicity estimators. Other metallicity estimators calculated by PYMCZ are excluded from our analysis since they are not suitable for the case of SN 2018hti. In particular, Z94 (Zaritsky, Kennicutt & Huchra 1994) is valid only for the upper branch of the $\log_{10}R_{23}$ scale.[11] Also, the KD02 and KK04 methods should only be used for $\log_{10}(\mathrm{N2O2}) > -1.2$. The results are shown in the boxplot in Fig. 7 and are summarized in Table 1. As expected, the results point towards a metal-poor site with $12 + \log_{10}(\mathrm{O/H}) \approx 8.17$, which corresponds to a metallicity $Z \approx 0.3\ Z_\odot$ (assuming $12 + \log_{10}(\mathrm{O/H}) = 8.69$ for the solar metallicity, Asplund et al. 2009). This estimate nicely agrees with the results obtained by Lin et al. (2020a).

[10]The package can be found at https://github.com/nyusngroup/pyMCZ.

[11]The upper branch metallicity scale is defined by the condition $\log_{10}R_{23} < 0.9$ (e.g. Kewley & Ellison 2008).

Downloaded from https://academic.oup.com/mnras/article/512/3/4484/6549929 by Biblioteca Dipartimento di Scienze Economiche user on 06 February 2023

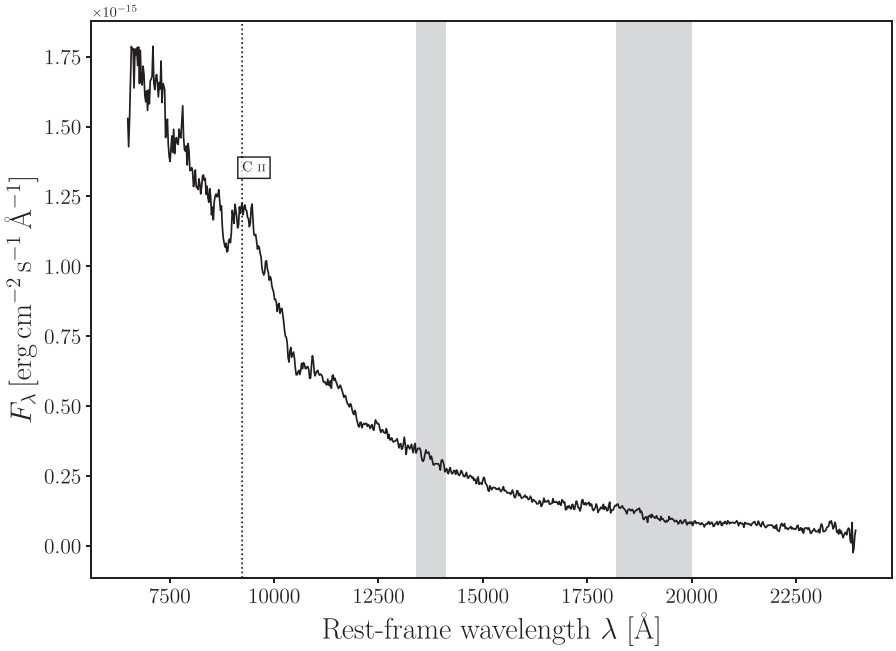


Figure 6. The IRTF+SpeX spectrum of SN 2018hti (black solid line). The black dotted line marks the C II at $\lambda = 9234$ Å line identification and the shaded grey areas mark the spectral regions corrected for telluric absorptions.

Moreover, we estimated the star formation rate (SFR) of the host galaxy of SN 2018hti based on the measurements of the flux emitted by the reddening-corrected narrow H α using equation 2 of Kennicutt (1998). The derived SFR is $\sim 0.3\,M_\odot\,yr^{-1}$, similar to the SFRs measured by Chen et al. (2017a) for a sample of galaxies hosting SLSNe I and comparable to the SFR of the Large Magellanic Cloud (Harris & Zaritsky 2009). Finally, we compared the values of SFR and metallicity of SN 2018hti with those of the comparison sample (see Table 2). Given the intrinsic uncertainty of these measurements, the selected SLSN-I sample seem to share similar environments, with the exception of SN 2015bn, which has an SFR about an order-of-magnitude lower than the others. However, as pointed out by Nicholl et al. (2015b), modelling the host-galaxy SED and estimating the median stellar mass and the age of the stellar population returns a higher SFR value of $0.55 \pm 0.18\,M_\odot\,yr^{-1}$ for SN 2015bn. Also, the SFR value reported for LSQ14bdq is an SFR limit (see also section 4 in Chen et al. 2017a).

4.2 Blackbody temperature and photospheric radius

We obtained the time evolution of the blackbody temperatures by fitting a blackbody curve to the spectra. This allow us to avoid the contribution of the spectral lines in the fitting procedure by excluding the line-contaminated regions from the fit domain. The comparison of the temperature evolution of SN 2018hti with SN 2015bn (Nicholl et al. 2016), SN 2006oz (Leloudas et al. 2012), iPTF13ehe (Yan et al. 2015, 2017b), iPTF15esb (Yan et al. 2017b), iPTF16bad (Yan et al. 2017b) is shown in Fig. 8 (left-hand panel). The data of SN 2006oz are relatively dispersed, but are useful for an order-of-magnitude comparison. The temperature evolution of SN 2018hti is essentially monotonic and is very similar to the case of SN 2006oz, the steepest of the sample. SN 2018hti and SN 2006oz appear to have the hottest photospheres among the SLSNe I sample. However, the scarcer sampling of the blackbody temperatures of iPTF13ehe and iPTF16bad do not allow to properly compare them with SN 2018hti. In particular, both SN 2015bn and iPTF15esb reach a 'temperature floor' (Nicholl et al. 2017b) of 5000–8000 K after ∼50–80 d after maximum luminosity (Fig. 8) similar to the sample analysed by Inserra et al. (2013) (see also Nicholl et al. 2017b). In the case of SN 2018hti it is unclear whether or not the temperature evolution actually settles on a plateau at that phase.

We also determine the evolution of the photospheric radius (Fig. 8, right-hand panel) R_{ph} using the Stefan–Boltzmann law, where we used the pseudo-bolometric luminosities shown in Fig. 4. To compare the more sparsely sampled spectroscopic epochs with those of the pseudo-bolometric luminosities, we fit the blackbody temperatures with a second-order polynomial. The photospheric radius of SN 2018hti monotonically grows to a maximum value of $\sim 9 \times 10^{15}$ cm in 100 d, which is about ∼50 d later the maximum bolometric luminosity. It then recedes at a rate of about 7×10^{13} cm^2 day^{-1}, which is similar to the average growth rate. Overall, the photospheric-radius evolution is consistent with the expansion radius determined from expansion velocity derived from some spectral lines (see Section 4.3) except for the time interval between −26 and 35 rest-frame days from maximum (see Fig. 8, right-hand panel). However, given the huge uncertainties, this should be considered only as an order-of-magnitude comparison. In the same figure we also show the photospheric-radius evolution of SN 2006oz. The photosphere of SN 2006oz seems less extended than that of SN 2018hti. In fact, given that both of them have a comparable photospheric temperature, SN 2006oz is about ∼0.5 mag fainter than SN 2018hti (see also Sec. 4.4).

4.3 Photospheric velocity

The photospheric velocity of SN 2018hti is measured via the O II λ 4357, O II λ 4650, and O I λ 7774 P-Cygni absorption features present in the spectra. In particular, it has been shown that the O I

Downloaded from https://academic.oup.com/mnras/article/512/3/4484/6549929 by Biblioteca Dipartimento di Scienze Economiche user on 06 February 2023

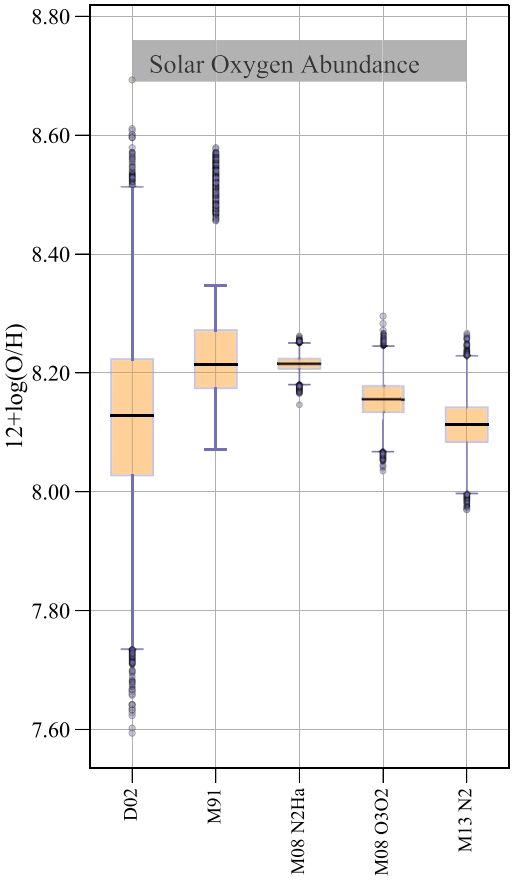


Figure 7. Boxplot obtained with the tool PYMCZ. The orange boxes cover the interquartile range (IQR) for each estimator, and the blue dots deviate from the first and third quartile more then 1.5 × IQR. The grey box broadly corresponds to the solar oxygen abundance.

Table 1. Metallicity estimators provided by the PYMCZ tool for the site of SN 2018hti (see also Fig. 7).

Estimator	$12+\log_{10}(O/H)$
D02	$8.128^{+0.142}_{-0.149}$
M91	$8.214^{+0.123}_{-0.055}$
M08_N2HA	$8.215^{+0.013}_{-0.013}$
M08_O3O2	$8.156^{+0.033}_{-0.033}$
M13_N2	$8.113^{+0.044}_{-0.042}$

λ 7774 feature is a good tracer of the photosphere of the stripped envelope SNe (Dessart et al. 2015). The wavelengths corresponding to the absorption minima were inferred from a Gaussian fit of the absorption features (see Fig. 9). This method is marginally affected by the line blending (Jeffery & Branch 1990) which can substantially bias the velocity measurements (Gal-Yam 2019b). The velocity evolution of SN 2018hti is shown in Fig. 10 (right-hand panel) in comparison with the photospheric velocities of SN 2015bn, iPTF13ehe, iPTF15esb, and iPTF16bad (where the photospheric velocities of iPTF13ehe, iPTF15esb, and iPTF16bad were retrieved based on the Fe II λ 5169). In the case of SN 2018hti, after an initial very steep decline, the velocity evolution settles on an early plateau which starts ∼22 d before maximum luminosity and lasts ∼30 d. Overall, the photosphere of SN 2018hti recedes (in mass coordinates) similarly to SN 2015bn and both of them are much slower than the other SLSNe I of the comparison sample. Finally, we compared the photospheric-velocity evolution of SN 2018hti with the results of the numerical radiation hydrodynamic calculations of Kasen & Bildsten (2010, see also their fig. 2, bottom panel) for a magnetar-powered SN assuming a magnetic field $B_p = 0.5 \times 10^{14}$ G, an initial period $P_{spin} = 5$ ms, an ejecta mass $M_{ejecta} = 5\,M_\odot$, and a kinetic energy $E_{kin} = 10^{51}$ erg. We scaled this solution by a factor 1.37 to almost perfectly fit the measured photospheric velocities of SN 2018hti (see also Section 4.5.2).

4.4 Comparisons with other SLSNe I

We compared the *r*-filter absolute magnitude LC of SN 2018hti with those of the comparison sample (see Fig. 11, left-hand panel). These SLSNe I show an early bump in their LCs and/or spectral signatures that likely involve some ejecta-CSM interaction (i.e. a possible Hα emergence). Interestingly, this sample shares similar evolutionary time-scales (see Fig. 11, left-hand panel) up to ∼80 d after maximum light, even though the absolute peak magnitude spans a range >2 mag.

Three representative spectra of SN 2018hti (at phases −8, +73, +269 d after maximum) are compared with the spectra of LSQ14bdq, SN 2018bsz, DES14X3taz, Gaia16apd, and SN 2015bn (Fig. 12). The spectra of LSQ14bdq, 2018bsz, iPTF15esb, Gaia16apd, DES14X3taz, and SN 2015bn are from WISEREP[12] (Yaron & Gal-Yam 2012). The spectrum of SN 2018hti taken 8 d prior to maximum light is compared with the spectra of LSQ14bdq (at a phase of −15 rest-frame days), SN 2018bsz (at a phase of −6 rest-frame days), and DES14X3taz (at a phase of −21 rest-frame days). At these phases, the O II features in the blue region of the spectrum of SN 2018hti nicely match those of LSQ14bdq, SN 2018bsz, and DES14X3taz. However, in the earliest spectrum of SN 2018bsz the P-Cygni maximum of the O II λ 4650 feature is likely affected by line blending with C II λ 4745 (Anderson et al. 2018). At about 60–70 d after maximum luminosity, the spectrum of SN 2018hti is also similar to the spectrum of iPTF15esb, although the latter shows a more prominent Mg I] λ 4571 and broader Fe-group features at ∼5500 Å. The remarkable resemblance between SN 2018hti and SN 2015bn at about 70 d after maximum suggests that these SNe have similar ejecta velocities (see also Fig. 10) and chemical composition. Finally, the late/pseudo-nebular spectrum of SN 2018hti at 269 d after maximum is compared with the spectra of SN 2015bn and Gaia16apd at a phase +270 and +252 d, respectively. The nebular emission features of SN 2015bn and Gaia16apd are more strongly developed compared to SN 2018hti, although they share some resemblance in the blue region of the spectrum.

4.5 Data interpretation

We considered two different scenarios to interpret the data of SN 2018hti: the magnetar and the ejecta-CSM interaction scenarios. To test the viability of the two hypotheses, we modelled the multicolour LCs of SN 2018hti with the Modular Open Source Fitter for Transients (MOSFIT, Guillochon et al. 2017, 2018). We also used the published radiative-transfer solutions of the SUMO code (Jerkstrand et al. 2017) for the nebular emission of O-zone material

[12] https://wiserep.weizmann.ac.il.

Downloaded from https://academic.oup.com/mnras/article/512/3/4484/6549929 by Biblioteca Dipartimento di Scienze Economiche user on 06 February 2023

Table 2. Metallicities and SFRs of the SLSNe I of the comparison sample as published in literature.

	SN 2018hti	LSQ14bdq	SN 2015bn	SN 2006oz	DES14X3taz
$Z/Z_{\odot}$	**0.3**	–	0.2 (Nicholl et al. 2016)	0.5 (Leloudas et al. 2012)	–
SFR [$M_{\odot}$ yr^{-1}]	**0.3**	<0.05 (Chen et al. 2017a)	0.04 (Nicholl et al. 2016)	0.17 (Leloudas et al. 2012)	0.16 (Smith et al. 2016)

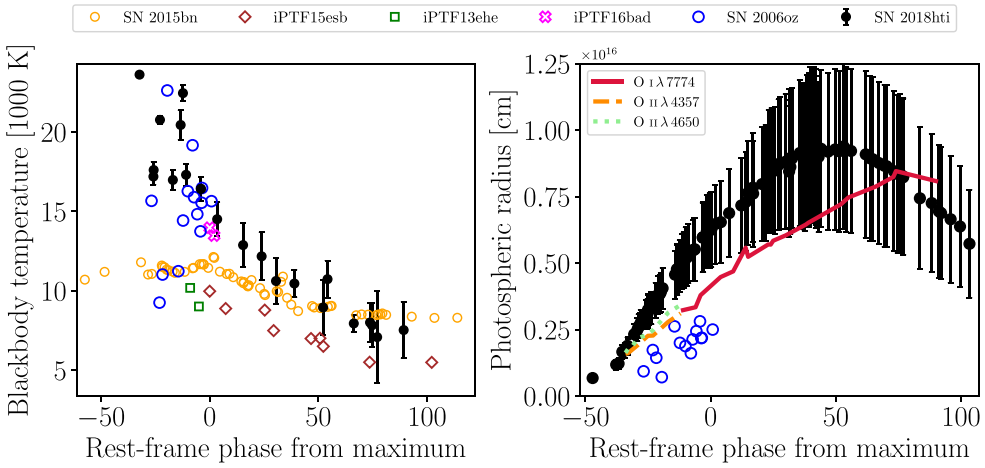


Figure 8. Left-hand panel: the blackbody temperatures of SN 2018hti (black filled dots). The blackbody temperature evolution of SN 2015bn (orange empty dots, Nicholl et al. 2016), SN 2006oz (blue empty dots, Leloudas et al. 2012), iPTF13ehe (green empty squares, Yan et al. 2015, 2017b), iPTF15esb (brown empty diamonds, Yan et al. 2017b), and iPTF16bad (magenta empty crosses, Yan et al. 2017b) are also shown for comparison. Right-hand panel: the evolution of the photospheric radius of SN 2018hti (black dots) compared with SN 2006oz. For comparison we also plot the radius obtained from the photospheric-velocity measurements performed on the spectra for the O I (red solid line) and the O II absorptions (λ 4357, orange dashed line, λ 4650, green dotted line).

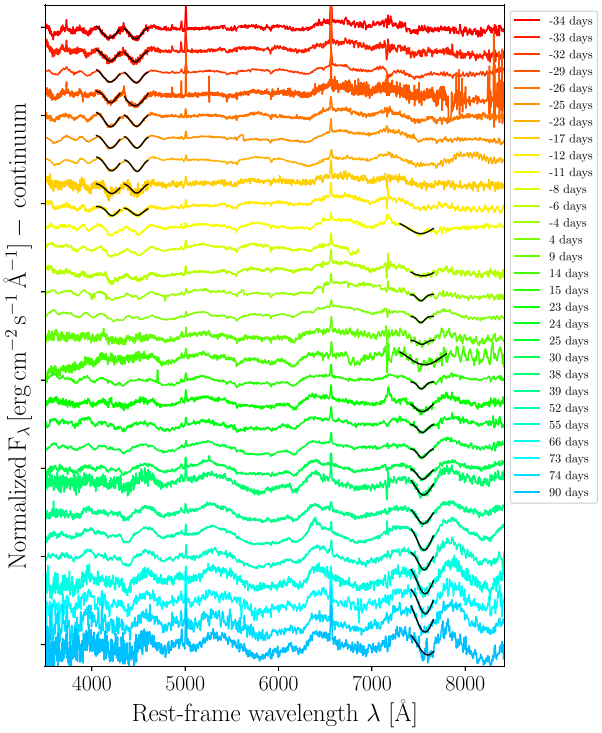


Figure 9. Normalized and continuum-subtracted spectra of SN 2018hti. A Gaussian curve (black solid line) is fitted to the absorption minima of the O II λλ 4357,4650 and the O I λ 7774 features. For the epochs in which more than one spectrum is available, we chose the spectrum with the greatest signal-to-noise ratio.

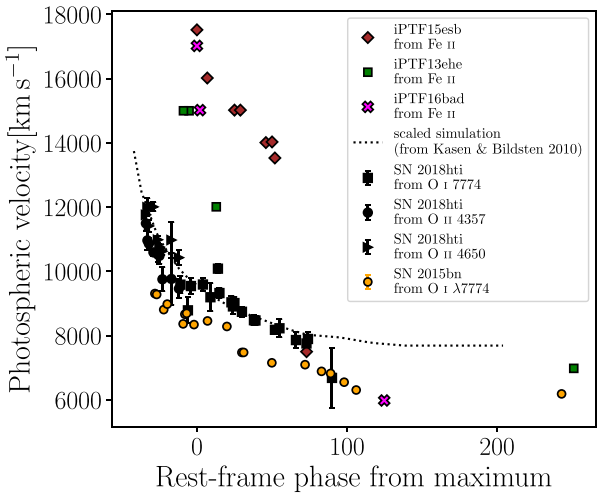


Figure 10. Photospheric velocities of SN 2018hti deduced from the absorption minima of O II λλ 4357,4650 (black dots and triangles) and O I λ 7774 (black squares) P-Cygni profiles (see the text). The evolution of the photospheric velocity of SN 2015bn (deduced by the O I, data taken from Nicholl et al. 2016, yellow dots), iPTF13ehe (green squares), iPTF15esb (brown diamonds), and iPTF16bad (magenta crosses) (deduced by the Fe II, Yan et al. 2017b) are shown for comparison. We also compared the photospheric velocity of SN 2018hti with the prediction of Kasen & Bildsten (2010) for a magnetar-powered SN (black dotted line, see the text).

Downloaded from https://academic.oup.com/mnras/article/512/3/4484/6549929 by Biblioteca Dipartimento di Scienze Economiche user on 06 February 2023

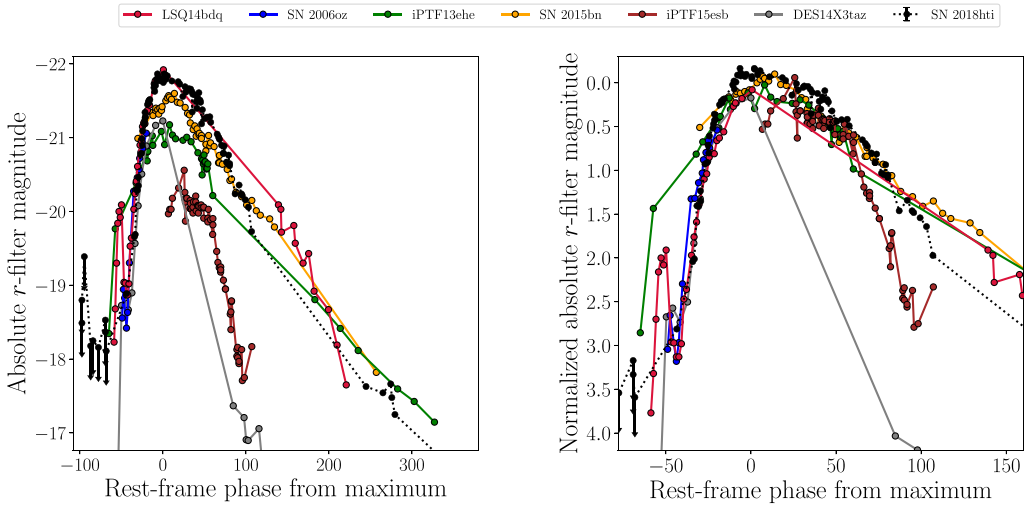


Figure 11. Left-hand panel: comparison of the *r*-filter absolute magnitude LC of SN 2018hti with those of LSQ14bdq (red dots), SN 2006oz (blue dots), iPTF13ehe (green dots), SN 2015bn (yellow dots), iPTF15esb (brown dots), and DES14X3taz (grey dots). Right-hand panel: same as the left-hand panel, but with the LCs normalized to maximum luminosity. Absolute magnitudes were corrected for Galactic extinction as in Section 2 and calculated with the assumed cosmology in this work. Where *K*-correction values were not available, we assume a constant *K*-correction $2.5\log(1+z)$.

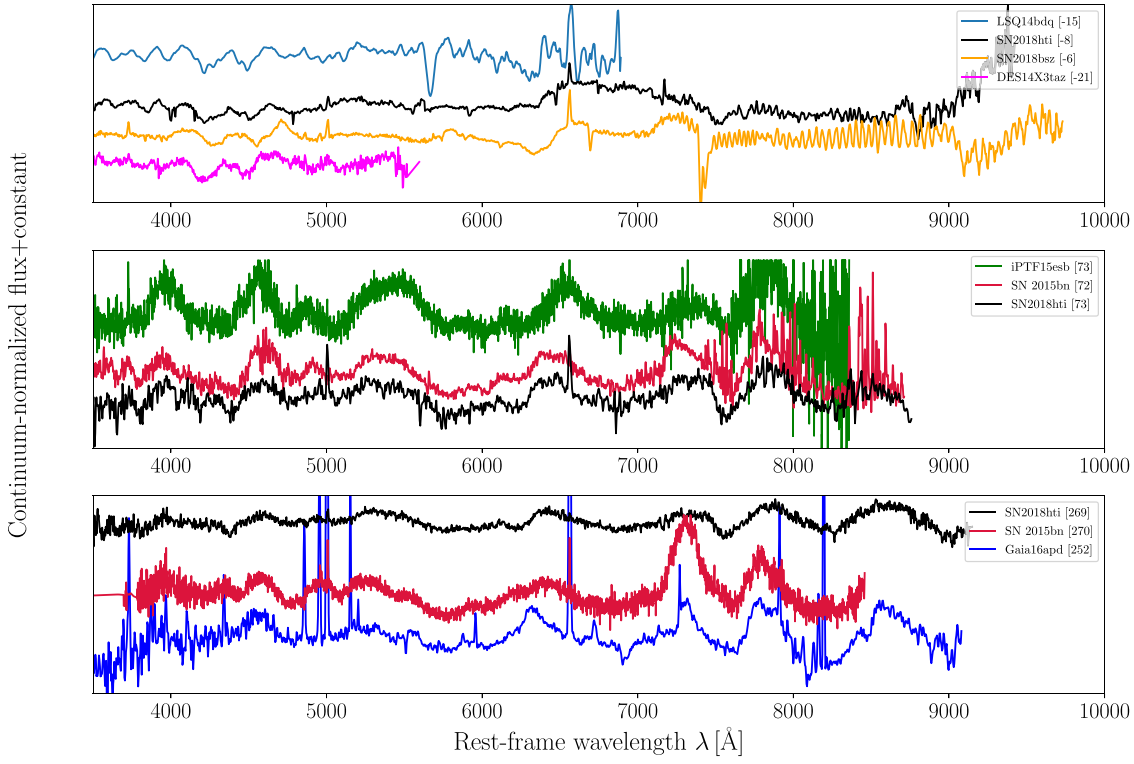


Figure 12. Comparisons of three spectra of SN 2018hti at different phases with respect to maximum luminosity (the rest-frame phase from maximum luminosity is indicated among square brackets in the legend). Upper panel: comparison among SN 2018hti (8 d before maximum, black line), SN 2018bsz (13 d before maximum, Anderson et al. 2018), LSQ14bdq (15 d before maximum, light blue line, see Nicholl et al. 2015b), and DES14X3taz (21 rest-frame days before maximum, magenta line, Smith et al. 2016). Middle panel: comparison among SN 2018hti (73 rest-frame days after maximum, black line), SN 2015bn (72 rest-frame days after maximum, red line), and iPTF15esb (73 rest-frame days from maximum, green line, see Yan et al. 2017b). Lower panel: comparison between SN 2018hti (269 rest-frame days after maximum, black line), SN 2015bn (270 rest-frame days after maximum, red line, see Nicholl et al. 2016), and Gaia16apd (252 rest-frame days after maximum, blue line, Kangas et al. 2017). For a better visualization, the spectrum of LSQ14bdq was smoothed with a Savitzki-Golay filter due to its lower signal-to-noise ratio. The spectra of iPTF15esb, 2018bsz, LSQ14bdq, SN 2015bn, and of Gaia16apd were obtained via WISEREP.

Downloaded from https://academic.oup.com/mnras/article/512/3/4484/6549929 by Biblioteca Dipartimento di Scienze Economiche user on 06 February 2023